






RESEARCH ARTICLE | NOVEMBER 08 2023

Estimation of the elastic and piezoelectric tensors of sapphire and lithium niobate from Brillouin light backscattering measurements of a single crystal sample

Fehima Ugarak ; Julio A. Iglesias Martínez ; Alexis Mosset ; Vincent Laude  



J. Appl. Phys. 134, 185103 (2023)

<https://doi.org/10.1063/5.0169889>



View Online



Export Citation

CrossMark

AIP Advances

Why Publish With Us?

-  **25 DAYS**
average time to 1st decision
-  **740+ DOWNLOADS**
average per article
-  **INCLUSIVE**
scope

[Learn More](#)



Estimation of the elastic and piezoelectric tensors of sapphire and lithium niobate from Brillouin light backscattering measurements of a single crystal sample

Cite as: J. Appl. Phys. **134**, 185103 (2023); doi: [10.1063/5.0169889](https://doi.org/10.1063/5.0169889)

Submitted: 29 July 2023 · Accepted: 19 October 2023 ·

Published Online: 8 November 2023



View Online



Export Citation



CrossMark

Fehima Ugarak,  Julio A. Iglesias Martínez,  Alexis Mosset,  and Vincent Laude^{a)} 

AFFILIATIONS

Université de Franche-Comté, CNRS, Institut FEMTO-ST, F-25000 Besançon, France

^{a)}Author to whom correspondence should be addressed: vincent.laude@femto-st.fr

ABSTRACT

Brillouin light scattering is a versatile measurement technique of the dispersion of bulk acoustic phonons in amorphous and crystalline solids. It allows contactless and non-destructive characterization of the relevant material tensors of optically transparent materials, provided that the optical refraction indices, and in addition the dielectric tensor for piezoelectric materials, are known beforehand. The complete estimation of the anisotropic material tensors is often performed using many different crystal orientations, and hence different samples of the same crystal. In this paper, we consider the problem of measuring those tensors using a single sample of an anisotropic single crystal with trigonal symmetry. A complete measurement requires sufficient experimental diversity in the phonon wavevectors when sampling the phonon velocity surfaces, hence the consideration of a large number of directions away from crystallographic axes. We estimate all six independent elastic constants of non-piezoelectric sapphire (3 m point group) with a single X-cut wafer and the six independent elastic constants together with the four independent piezoelectric constants of piezoelectric lithium niobate (3 m point group) with a single Y-cut wafer. The estimated tensors are in close agreement with those reported in the literature based on resonant ultrasonic techniques.

Published under an exclusive license by AIP Publishing. <https://doi.org/10.1063/5.0169889>

I. INTRODUCTION

Ultrasonic properties of solids are described by material tensors entering the constitutive relations of elasticity, piezoelectricity, photoelasticity, and more intricate models.^{1,2} Modern design and numerical simulation tools require those material tensors to be known to produce accurate results.³ Elastic, dielectric, and piezoelectric constants are available in the literature for many solids and were obtained as a result of many experimental studies over the last seventy years. They were obtained using different techniques and show some dispersion in the reported values. In this paper, we focus on two trigonal crystals, non-piezoelectric 3 m sapphire and piezoelectric 3 m lithium niobate, with the goal of estimating all elastic and piezoelectric constants from the non-contact measurement of a single piece of wafer with known orientation.

The reported properties of lithium niobate were obtained using different techniques. O'Brien *et al.*⁴ reported elastic and

piezoelectric properties obtained using the Brillouin light scattering (BLS) technique for bulk phonons in samples with different orientations oriented along pure crystalline directions. The measurements in the present work also rely on bulk BLS measurements,^{5–8} but with a single Y-cut wafer, and rely on a variety of phonon wave vectors to sample the acoustic phonon velocity surfaces. Smith and Welsh⁹ performed ultrasonic phase-velocity measurements of the resonances of bar and plate samples. Kovacs *et al.*¹⁰ performed surface acoustic wave (SAW) measurements using a laser Doppler vibrometer and a set of transducers on a single wafer of lithium niobate with 128° rot Y-cut wafer. Ogi *et al.*¹¹ employed acoustic spectroscopy to characterize the resonances of a single crystal specimen.

As sapphire is not piezoelectric, the electric generation of elastic waves is indirect, via the bonding of an external transducer onto the specimens. Mayer and Hiedemann¹² measured the ultrasonic velocities in a certain crystallographic direction based on a

11 November 2023 17:04:12

combination of three optical methods. Wachtman *et al.*¹³ measured the elastic resonances of two rectangular block specimens of corundum (synthetic sapphire) and observed that the values obtained differed from those obtained previously, including early similar investigations by Rao¹⁴ and Bhimasenachar¹⁵ for synthetic and natural sapphire, respectively. Bernstein¹⁶ performed pulse-echo measurements on three sapphire blocks and compared them to resonance measurements on the same samples, obtaining two different but close sets of elastic constants. Gladden *et al.*¹⁷ employed resonant ultrasound spectroscopy to ascertain all independent elastic constants. They found the sign of the elastic constant c_{14} to be positive, in contrast to previous reports. Hovis *et al.*¹⁸ confirmed this sign using x-ray residual stress measurements. We are unaware of the complete determination of the elastic constants of sapphire using bulk BLS measurements, as we report in this paper with a single X-cut wafer.

BLS,¹⁹ as a non-destructive and contactless characterization technique, enables one to measure the elastic^{20–22} and piezoelectric properties^{23,24} precisely from the phase velocity of bulk phonons,^{25,26} provided optical indices of refraction are known. The measurement of piezoelectric properties further requires knowledge of the low-frequency dielectric tensor. Compared to resonant ultrasonic techniques, the BLS frequencies of bulk acoustic phonons are independent of sample dimensions and boundary conditions. We emphasize that the estimation of the full elastic tensor, for both sapphire and lithium niobate samples, is obtained in this work from a single wafer, whereas conventionally a selection of different, simple crystal orientations is considered.¹⁹ The fitting procedure we use is instead based on the measurement of phonon velocities along a set of different, arbitrary wavevector directions that are not aligned with simple crystallographic directions and that sample the phonon velocity surfaces. For successful estimation of material tensors, it is necessary to have sufficient diversity in the experimental data so that all independent tensor elements are represented. Considering only a portion of the XY and XZ incidence planes for sapphire, and the YX and YZ incidence planes for lithium niobate, was found to be sufficient in this respect. A comparison with previously reported values for material tensors of sapphire and lithium niobate is presented, both using tables of numerical values and a graphical comparison of measurements with computed phonon velocity surfaces.

II. METHODS

A. Experimental setup

Figure 1 depicts the experimental BLS setup. A longitudinal single-mode laser with a wavelength of $\lambda_0 = 532$ nm is used as the source of incident photons. The laser provides linearly polarized light (represented with a black dot in Fig. 1). The beam splitter splits the beam into two paths. The reference path (dashed line) is used for the alignment and remote control of the Fabry–Pérot interferometers,²⁷ whereas the main path is used for characterization of the sample.

The power of the main light beam is adjusted with a neutral density filter in order to provide enough backscattered photons while avoiding damage of the sample or saturation of the detector. After reflection on alignment mirrors M1 and M2, the incident

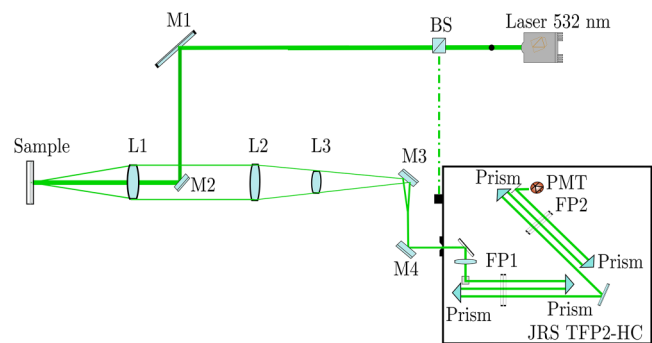


FIG. 1. Setup used for Brillouin light backscattering measurements. BS: beam splitter; M1–M4: mirrors; L1–L3: lenses; FP1: Fabry–Pérot 1; FP2: Fabry–Pérot 2; PMT: Photodetector.

laser beam is focused on the sample using lens L1 (focal length $f_1 = 100$ mm). The spot diameter on the sample is about $50 \mu\text{m}$. Backscattered light is collected by the same lens (numerical aperture $\text{NA} = 0.1$) and imaged by a manually built Keplerian beam expander including lenses L2 and L3 (focal lengths $f_2 = 100$ mm and $f_3 = 30$ mm). Mirrors M3 and M4 are adjusted so that the main light beam enters precisely the entrance pinhole of the Sandercock-type 3+3-pass tandem Fabry–Pérot interferometer (TFP2-HC manufactured by JRS) with the aperture of $600 \mu\text{m}$ with previously adjusted mirror spacings of 1.5 and 2 mm and scanning amplitudes 450 nm for sapphire and 470 nm for lithium niobate, respectively. The total finesse of the tandem Fabry–Pérot interferometer is 100.

The reference beam, with a maximum power of 1 mW, gives the central line in the spectrum, or Rayleigh scattering elastic peak. A shutter system is inserted in front of the entrance pinhole and switches automatically to the reference signal during the part of the scan that corresponds to the transmission of elastically scattered light. This arrangement avoids a possible overload by the intense elastically scattered light and potential damage to the detector. The very weak signal, produced by the spontaneous inelastic scattering of light by bulk phonons, is filtered with a high contrast ratio ($> 10^9$), detected by a synchronized photomultiplier and processed by a multi-channel analyzer with 512 channels (model MCA-1, The Table Stable LTD). Further spectrum analysis is performed using software GHOST 7.00 (The Table Stable LTD).

As the elastic and optical properties of anisotropic materials are angle dependent, the holder of the sample can be rotated to define precisely a direction in 3D space with a homemade (Labview) interface. The incidence angle ϕ , defined in Fig. 2(a), is the angle between the incident beam and the normal to the surface of the sample. In addition, the sample can be rotated around the normal to the surface by angle ψ . The pair (ψ, ϕ) defines the direction of optical incidence with respect to the sample. The backscattering arrangement imposes that the direction of scattered light is colinear with the incident light and makes an angle π with it.²⁸ The backscattering arrangement provides a comparably large interaction volume, allowing for a high temporal resolution and Brillouin

11 November 2023 17:04:12

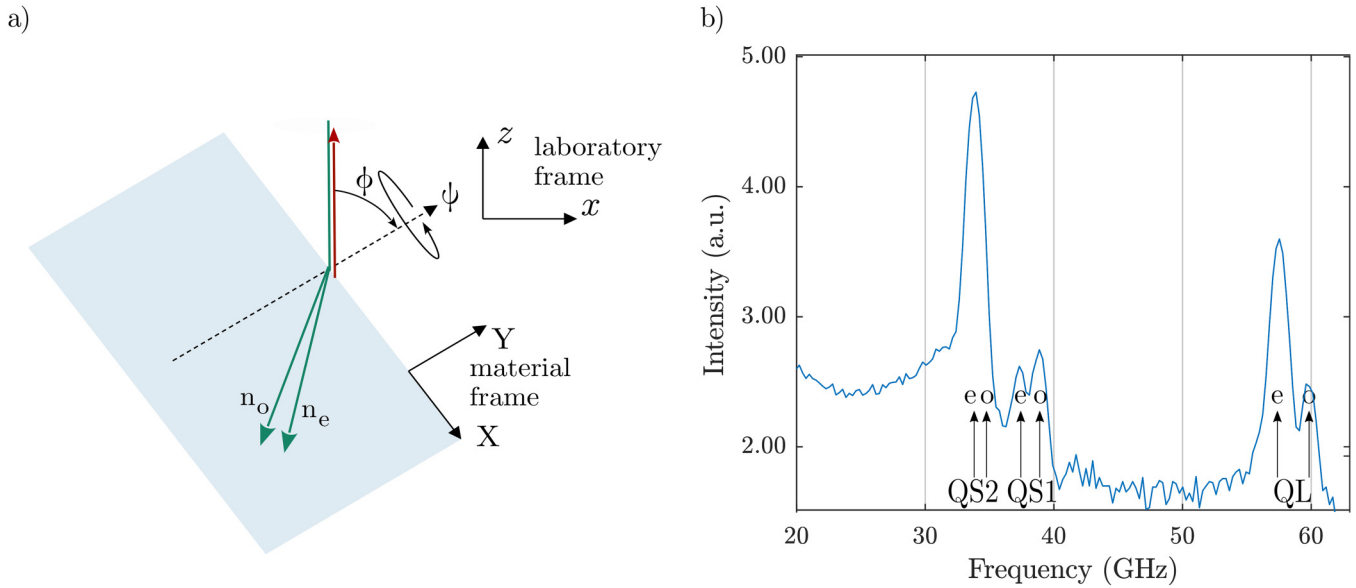


FIG. 2. Brillouin light scattering in birefringent crystals. (a) Angles of rotation for the sample in Brillouin Light backscattering configuration with laboratory and material frame where birefringence implies two independent optical modes of propagation. (b) BLS response from lithium niobate (cut YX, $\phi = 2^\circ$, $\psi = 45^\circ$) where up to six phonon peaks appear [two for quasi-longitudinal wave (QL), two for quasi-shear wave 1 (QS1), and two for quasi-shear wave 2 (QS2)].

spectra that are recorded faster compared to other common scattering geometries.²⁹ The direction and magnitude of the acoustic wavevector \mathbf{q} are determined by the scattering geometry, which is extremely important in the case of material with preferential directions as in crystals and fibers.^{22,30–33}

Conservation of momentum for photons and phonons imposes the phase-matching condition between the interacting waves,

$$\mathbf{q} = \pm(\mathbf{k}_i - \mathbf{k}_s), \quad (1)$$

where \mathbf{k}_i is the incident wavevector and \mathbf{k}_s is the scattered wavevector, and the sign distinguishes between Stokes (+) and anti-Stokes (−) phonons. In a purely spontaneous Brillouin process, it is expected statistically that Stokes and anti-Stokes phonons contribute equally to the backscattered signal. In the backscattering configuration, $\mathbf{q} = \pm 2\mathbf{k}_i$ is directly dictated by the incidence direction and the laser wavelength.

B. Phonon dispersion

In a homogeneous anisotropic material, three acoustic phonons propagate in a given direction and define three closed velocity surfaces. The quasi-longitudinal phonon corresponds mostly to compression-expansion of the medium in the direction of propagation. The other two phonons represent collective shear vibrations that occur mostly perpendicularly to the propagation direction; they are termed quasi-shear phonons.² The BLS technique provides frequency shifts in the scattered light that are proportional to the phase velocities of the phonons, provided the

photoelastic effect does not vanish. Indeed, the phonon wavevector being imposed by (1), the phonon frequencies are given by the dispersion relation for bulk elastic waves $\omega = v|\mathbf{q}|$. In the backscattering configuration, $\omega/(2\pi) = 2vn/\lambda_0$ with n being the optical index of refraction. The phonon velocities v can be obtained by solving the Christoffel Eq. (3) for a harmonic plane wave³⁴ of the form

$$u_i(t, \mathbf{r}) = \hat{u}_i \exp(i(\omega t - \mathbf{q} \cdot \mathbf{r})). \quad (2)$$

Propagation is directed along normal vector $\hat{\mathbf{n}} = \mathbf{q}/|\mathbf{q}|$. The Christoffel equation provides an eigenvalue problem for the square of the velocity in a given direction,

$$\Gamma_{il} \hat{u}_l = \rho v^2 \hat{u}_i, \quad (3)$$

with ρ being the density of mass. For a non-piezoelectric material, for instance sapphire, $\Gamma_{il} = c_{ijkl} \hat{n}_j \hat{n}_k$ depends only on the elastic tensor c_{ijkl} . For a piezoelectric material, for instance, lithium niobate, Christoffel's tensor is modified to

$$\Gamma_{il} = c_{ijkl} \hat{n}_j \hat{n}_k + \frac{\gamma_i \gamma_l}{\epsilon}, \quad (4)$$

where $\gamma_i = e_{kij} \hat{n}_j \hat{n}_k$ and $\epsilon = \epsilon_{jkl} \hat{n}_j \hat{n}_k$; e_{kij} is the piezoelectric tensor and ϵ_{jkl} is the dielectric tensor. Phonon velocities hence depend on the ratio of effective piezoelectric constants to the effective dielectric constant, implying that the latter must be determined otherwise in BLS measurements.

11 November 2023 17:04:12

C. Brillouin light scattering in optically birefringent media

Brillouin light scattering is a photon–phonon interaction that occurs within the material under study. We consider two different frames to describe it. The material frame in Fig. 2(a) is attached to the sample and describes the particular crystal cut. The example depicted is for a Y-cut wafer (the normal to the surface is along the Y crystallographic axis). The laboratory frame is used to describe the orientation of the sample in space, based on angles (ψ, ϕ) . By definition, axis z is the incident and backscattering direction and the laser light is linearly polarized along axis y .

Both sapphire and lithium niobate are negative uniaxial crystals. For lithium niobate,³⁵ the extraordinary refraction index $n_e = 2.2320$ and the ordinary refraction index $n_o = 2.3210$ (for sapphire,³⁶ $n_e = 1.7636$ and $n_o = 1.7717$), at $\lambda_0 = 532$ nm. In a birefringent medium, incident light is decomposed into two refracted ordinary and extraordinary modes of propagation with different refraction angles, as Fig. 2(a) depicts. As a result, there are at most six different BLS peaks in the response, for two incident photons and three acoustic phonons. The example of Fig. 2(b), for Y-cut lithium niobate with $\phi = 2^\circ$ and $\psi = 45^\circ$, shows five different BLS peaks (the ordinary-QS2 peak is not clearly apparent). The difference in ordinary and extraordinary optical indices, or birefringence, is about 5%, leading to a similar separation of the pairs of peaks. In the case of sapphire, the birefringence is less than 0.6% and the ordinary and extraordinary peaks would be hardly distinguishable experimentally, given the frequency resolution of the interferometer.

A wrong classification of ordinary or extraordinary contributions to the BLS spectrum may lead to errors in the estimation of material tensors. For this reason, we consider only optical polarizations along a pure crystallographic axis of the crystal. For Y-cut lithium niobate, the y axis is either aligned with the X axis ($\psi = 0$) or with the $-Z$ axis ($\psi = \pi/2$). For X-cut sapphire, the y axis is either aligned with the Y axis ($\psi = 0$) or with the Z axis ($\psi = \pi/2$). With this arrangement, the optical polarization remains, in principle, the same as the angle of incidence ϕ is changed.

The relative efficiency of the Brillouin process depends on the photoelastic characteristics. Certain phonon contributions may be absent from the BLS spectra if the photoelastic efficiency vanishes by symmetry or if it is too small in magnitude. As an estimation of this efficiency, we use the formula for spontaneous Brillouin scattering,¹⁹

$$P_{\text{eff}} = p_{ijkl} E_i E_j u_k \frac{q_l}{|\mathbf{q}|} \sqrt{\frac{k_B T}{\rho}} \frac{1}{v} n_{\text{eff}}^3, \quad (5)$$

where p_{ijkl} is the photoelastic tensor, u_k are the components of a unit vector describing phonon polarization, E_i and E_j are components of unit vectors representing the polarization of the incident and scattered electric fields, k_B is the Boltzmann constant, T is the temperature, and n_{eff} is the effective optical index (equal to either n_o or n_e for optical polarizations along the pure crystallographic axis of the crystal). In practice, the variation of this quantity with the incidence angle is used to check which peaks should be observable in measurements. As a note, photoelastic constants are taken from Ref. 37 for sapphire and Ref. 35 for lithium niobate.

D. Estimation of material tensors for trigonal crystals

We wish to estimate from BLS spectra the material tensors, or rather their sets of independent constants. We use in the following the Voigt notation for symmetric pairs of indices, $I = (ij)$ and $J = (kl)$. Trigonal crystals with $\bar{3}m$ or $3m$ point-group symmetry have six independent elastic stiffness coefficients,

$$c_{IJ} = \begin{bmatrix} c_{11} & c_{12} & c_{13} & c_{14} & 0 & 0 \\ c_{12} & c_{11} & c_{13} & -c_{14} & 0 & 0 \\ c_{13} & c_{13} & c_{33} & 0 & 0 & 0 \\ c_{14} & -c_{14} & 0 & c_{44} & 0 & 0 \\ 0 & 0 & 0 & 0 & c_{44} & c_{14} \\ 0 & 0 & 0 & 0 & c_{14} & c_{66} \end{bmatrix}, \quad (6)$$

with $c_{66} = (c_{11} - c_{12})/2$. For $3m$ crystals, there are four independent piezoelectric constants,

$$e_{ij} = \begin{bmatrix} 0 & 0 & 0 & 0 & e_{15} & -e_{22} \\ -e_{22} & e_{22} & 0 & e_{33} & 0 & 0 \\ e_{31} & e_{31} & e_{33} & 0 & 0 & 0 \end{bmatrix}. \quad (7)$$

For $\bar{3}m$ crystals, $e_{ij} = 0$ because of centro-symmetry. The dielectric tensor (at low frequencies) has two independent constants,

$$\epsilon_{ij} = \begin{bmatrix} \epsilon_{11} & 0 & 0 \\ 0 & \epsilon_{11} & 0 \\ 0 & 0 & \epsilon_{33} \end{bmatrix}. \quad (8)$$

Finally, the optical dielectric tensor is

$$\epsilon_{ij} = \epsilon_0 \begin{bmatrix} n_o^2 & 0 & 0 \\ 0 & n_o^2 & 0 \\ 0 & 0 & n_e^2 \end{bmatrix}, \quad (9)$$

with n_o being the ordinary and n_e being the extraordinary indices of refraction.

For non-piezoelectric sapphire, we consider the $m = 6$ independent elastic constants for the fit against experimental values. For piezoelectric lithium niobate, we add the four independent piezoelectric constants, for a total of $m = 10$ fit variables. Hence, we consider that the optical and low-frequency dielectric tensors are known beforehand. Actually, optical indices can only be obtained from an optical measurement, independent of the BLS measurement. The low-frequency dielectric tensor, in turn, enters the Christoffel tensor for piezoelectric media, but only as a normalization of the squared piezoelectric effective values, see Eq. (4). The m fit variables are arranged in a vector \mathbf{p} .

The number of experimental Brillouin peak frequencies f_j is M ($j = 1, \dots, M$). The fitting error that is minimized is

$$E(\mathbf{p}) = \sum_{j=1}^M \left(f_j - f(\alpha_j, \psi_j, \phi_j; \mathbf{p}) \right)^2 / f_j, \quad (10)$$

where (ψ_j, ϕ_j) are the sampling angles, $\alpha_j \in \{QL, QS1, QS2\}$ is the classification of the acoustic phonon, and $f(\alpha, \psi, \phi; \mathbf{p})$ is a function giving the theoretical Brillouin frequencies. The fitting error has units of frequencies (Hz). The Levenberg–Marquardt algorithm is used to obtain the minimum of the error E , starting from a given

initial set of material constants. The standard deviation of each fitted parameter is evaluated as

$$\sigma_i = \sqrt{\frac{E(\mathbf{p}_0)}{DV_p^{-1}[i, i]}}, \quad i = 1, \dots, m, \quad (11)$$

where $E(\mathbf{p}_0)$ is the remaining error at the minimum \mathbf{p}_0 , V_p is the Hessian matrix at the minimum, and $D = M - m + 1$ stands for the number of degrees of freedom. As a note, the standard deviations are indicators for the quality of the fit, expressed in the same physical units as the fitted material parameters.

III. RESULTS AND DISCUSSION

A. X-cut sapphire

Figure 3 summarizes the experimental data used for sapphire. The particular specimen is a X-cut rectangular wafer (Codex International) with the Y and Z axes aligned with the sides of the rectangle. BLS measurements were performed for varying incidence angle ϕ for $\psi = 0^\circ$ (XZ incidence plane, ordinary optical polarization) and $\psi = 90^\circ$ (XY incidence plane, extraordinary optical polarization). Theoretical Brillouin frequencies, obtained for the fitted material constants, are shown with circular markers.

For the XZ plane, the phonon frequencies are in theory symmetric with respect to angle ϕ . All three phonons are observed in Figs. 3(a) and 3(b), though the shear peaks are very small for small values of angle ϕ . The theoretical Brillouin efficiency in Fig. 3(c) indeed vanishes for $\phi = 0$ for both shear phonons. Experimentally, the Brillouin efficiency for QS2 appears sufficient for both $\phi \geq 20^\circ$ and $\phi \leq -25^\circ$, but too small for $\phi \geq 50^\circ$ and $\phi \leq -55^\circ$. Similarly, the QS1 peaks appear for $\phi \geq 20^\circ$ and for $\phi \leq -25^\circ$. Overall, it appears that there is a threshold on the value of the Brillouin efficiency that must be overcome for the measurements to be significant enough to be kept in the fit process.

For the XY plane, the phonon frequencies are also in theory symmetric with respect to angle ϕ . The theoretical Brillouin efficiencies for shear phonons in Fig. 3(f) remain small for all values of incidence angle ϕ . Thus, only the QL Brillouin data for the XY plane were used for the fit.

The fitted elastic constants are listed in the last column of Table I, together with the standard deviations. Figure 4 shows the phonon velocity curves in the XZ and the XY planes, together with the experimental velocities used for the fit. The quality of the fit is visually quite good, in the sense that the velocity curves match well with experimental points. The remaining fit error is 11.1 MHz.

Figure 5 shows the velocity curves in the XZ and XY planes computed with the different sets of elastic constants summarized in Table I. The purpose is here to compare directly BLS experimental results with those curves that are indeed quite sensitive to the values of the elastic constants. The complete set of six independent elastic constants was first reported by Rao¹⁴ for synthetic sapphire and then by Bimasenachar¹⁵ for natural sapphire, who obtained similar values except for c_{33} . Those early results are quite far from our results for sapphire. Mayer and Hiedemann¹² redetermined the elastic constants for synthetic sapphire, obtaining rather different results, that remain, however, still far from our BLS results. The findings of Wachtman *et al.*¹³ and Bernstein¹⁶ align well with the

results presented in this paper, based on BLS. However, the more recent experiments conducted by Gladden *et al.*¹⁷ and Hovis *et al.*¹⁸ exhibit an even better agreement with our measurements. The most important distinction lies in the sign of the elastic constant c_{14} . We checked the effect of setting the sign of the starting value for c_{14} (with all sx equivalent constants being flipped together): the fitting results are obtained exactly with the same error and standard deviations. Furthermore, the sign of c_{14} never changes during optimization. Hence, we conclude that we can only find the modulus of c_{14} with the incidence planes we considered, but not its sign.

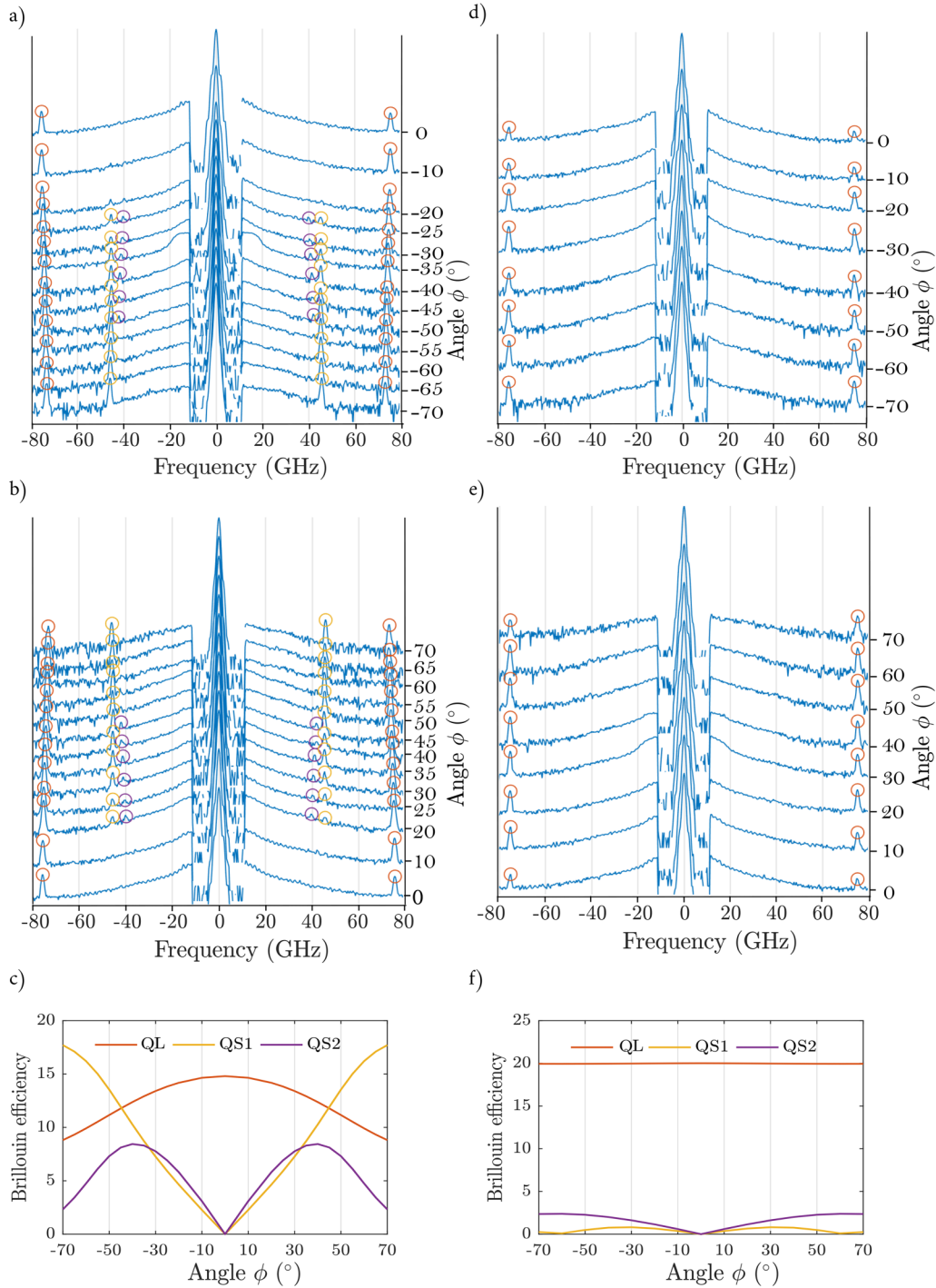
B. Y-cut lithium niobate

Figure 6 summarizes the experimental data used for lithium niobate. The particular specimen is a rectangular unpoled Y-cut wafer (Roditi) with the X axis and Z axis aligned with the sides of the rectangle. Measurements are presented for varying incidence angle ϕ for $\psi = 90^\circ$ (YZ incidence plane, ordinary optical polarization) and $\psi = 0^\circ$ (YX incidence plane, extraordinary optical polarization). Theoretical Brillouin frequencies, obtained for the fitted material constants, are shown with circular markers.

For the YZ plane, the phonon frequencies are not symmetric with respect to angle ϕ ; negative ϕ values are grouped in Fig. 6(a) whereas positive values are grouped in Fig. 6(b). All three phonons are observed for all values of angle ϕ . The theoretical Brillouin efficiency in Fig. 6(c) is relatively large for phonons QL and QS1 but vanishes for QS2 for all incidence angles, as a result of the symmetry of the photoelastic tensor. There is thus a discrepancy that must be accounted for. Alternatively, we made the hypothesis that the polarizer is not perfect but possesses a finite contrast ratio. Hence, it is possible that the polarization of light is not perfectly aligned with the X axis of the crystal but there is some part orthogonal to it. Since the photoelastic efficiency for extraordinary optical polarization is large, we thus assume that the QS2 frequency peaks are obtained for extraordinary index n_e and not for ordinary index n_o . In the fit, experimental QS2 frequencies were thus multiplied by a factor n_o/n_{eff} , where $n_{\text{eff}} = \sqrt{n_e^2 + (1 - (n_e/n_o)^2) \sin^2(\phi)^2}$, to account for this misclassification. As a note, the wavevector direction for the QS2 phonon also changes when the extraordinary wave is used for the interpretation instead of the ordinary wave, but the variation with ϕ is very small and was neglected.

For the YX plane, the phonon frequencies are in theory symmetric with angle ϕ ; only positive values were measured and are shown in Fig. 3(d). The theoretical Brillouin efficiencies for both QL and QS1 phonons in Fig. 6(e) are large, but the values for the QS2 phonons remain rather small for all values of incidence angle ϕ . They were, however, deemed sufficient and were kept in the fit process.

The fitted elastic and piezoelectric constants are listed in the last column of Table II, together with the standard deviations. Figure 7 shows the phonon velocity curves in the YZ and the YX planes, together with the experimental velocities used for the fit. The quality of the fit is visually very good, in the sense that the velocity curves match well with experimental points. The remaining fit error is 5.2 MHz.



11 November 2023 17:04:12

FIG. 3. BLS experimental results for a X-cut sapphire wafer. BLS spectra are shown for the XZ plane for (a) negative and (b) positive values of the angle of incidence ϕ . Theoretical phonon frequencies are shown with circular markers (orange: QL phonon; yellow: QS1 phonon; purple: QS2 phonon). The theoretical photoelastic response is shown in (c) as a function of the angle of incidence ϕ . BLS spectra are shown for the XY plane for (d) negative and (e) positive values of the angle of incidence ϕ . Theoretical phonon frequencies are shown with circular markers (orange: QL phonon; yellow: QS1 phonon; purple: QS2 phonon). The theoretical photoelastic response is shown in (f) as a function of the angle of incidence ϕ .

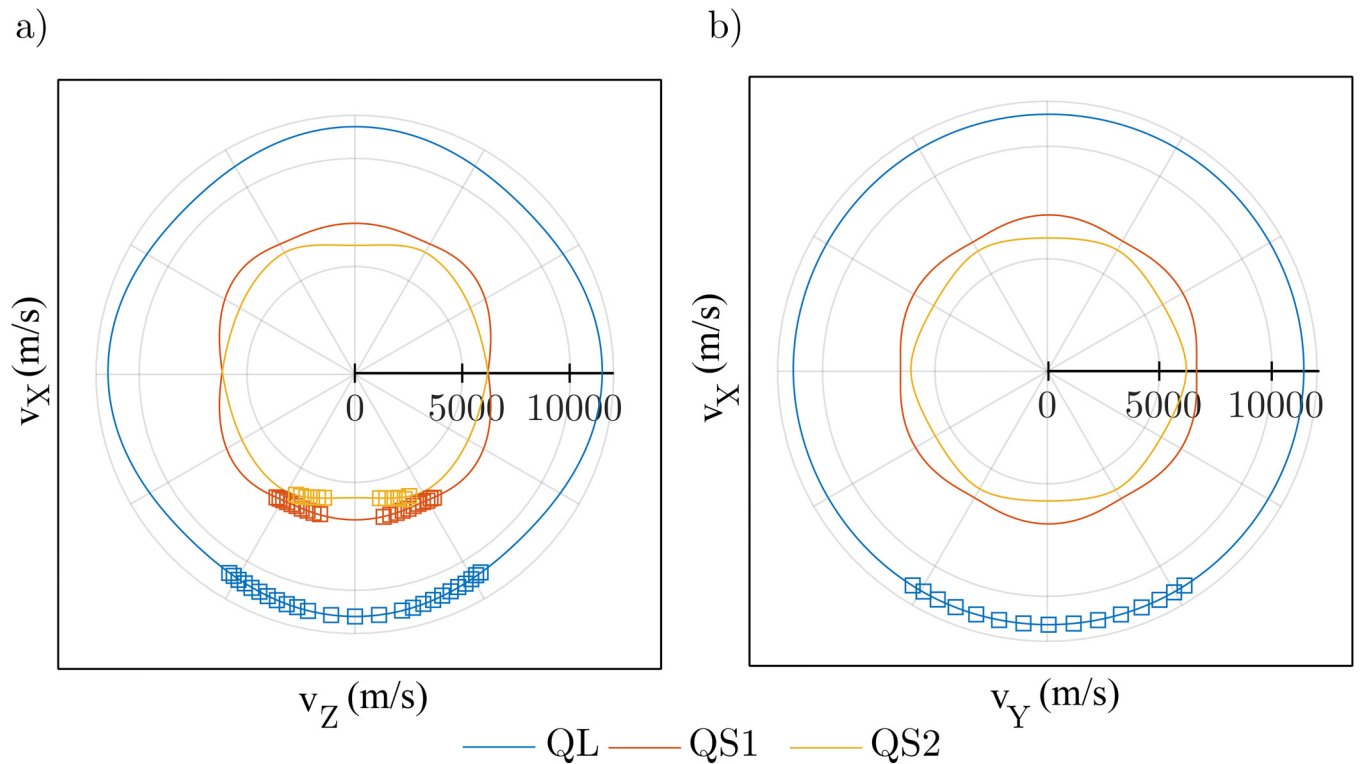
TABLE I. Independent material constants for sapphire, taken from the literature^{12,14–18} and obtained by fitting BLS measurements. Bernstein p. and r. stand, respectively, for Bernstein pulse-echo and resonance measurements.

	Elastic constants (GPa)								BLS
	Rao ¹⁴	Bhimasenachar ¹⁵	Mayer and Hiedemann ¹²	Wachtman <i>et al.</i> ¹³	Bernstein p. ¹⁶	Bernstein r. ¹⁶	Gladden ¹⁷	Hovis ¹⁸	
c_{11}	466.0	465.0	496.0	496.8	490.2	492.0	497.5	497.0	511.90 ± 0.21
c_{12}	127.0	124.0	109.0	163.6	165.4	168.4	162.7	163.0	166.65 ± 0.99
c_{13}	117.0	117.2	48.0	110.9	113.0	116.4	115.5	116.0	123.14 ± 1.24
c_{33}	506.0	563.0	502.0	498.1	490.2	492	503.3	501.0	522.54 ± 3.25
c_{44}	235.3	233.0	206.0	147.48	145.45	146.8	147.4	147.0	150.89 ± 0.68
c_{14}	9.4	101.0	38.0	-23.5	-23.2	-23.4	22.5	22.0	23.42 ± 0.15
	Remaining fit error (GHz)								0.0111

Figure 8 shows the velocity curves in the YZ and YX planes computed with the different sets of elastic and piezoelectric constants summarized in Table II. The purpose is here to compare directly BLS experimental results with those curves.

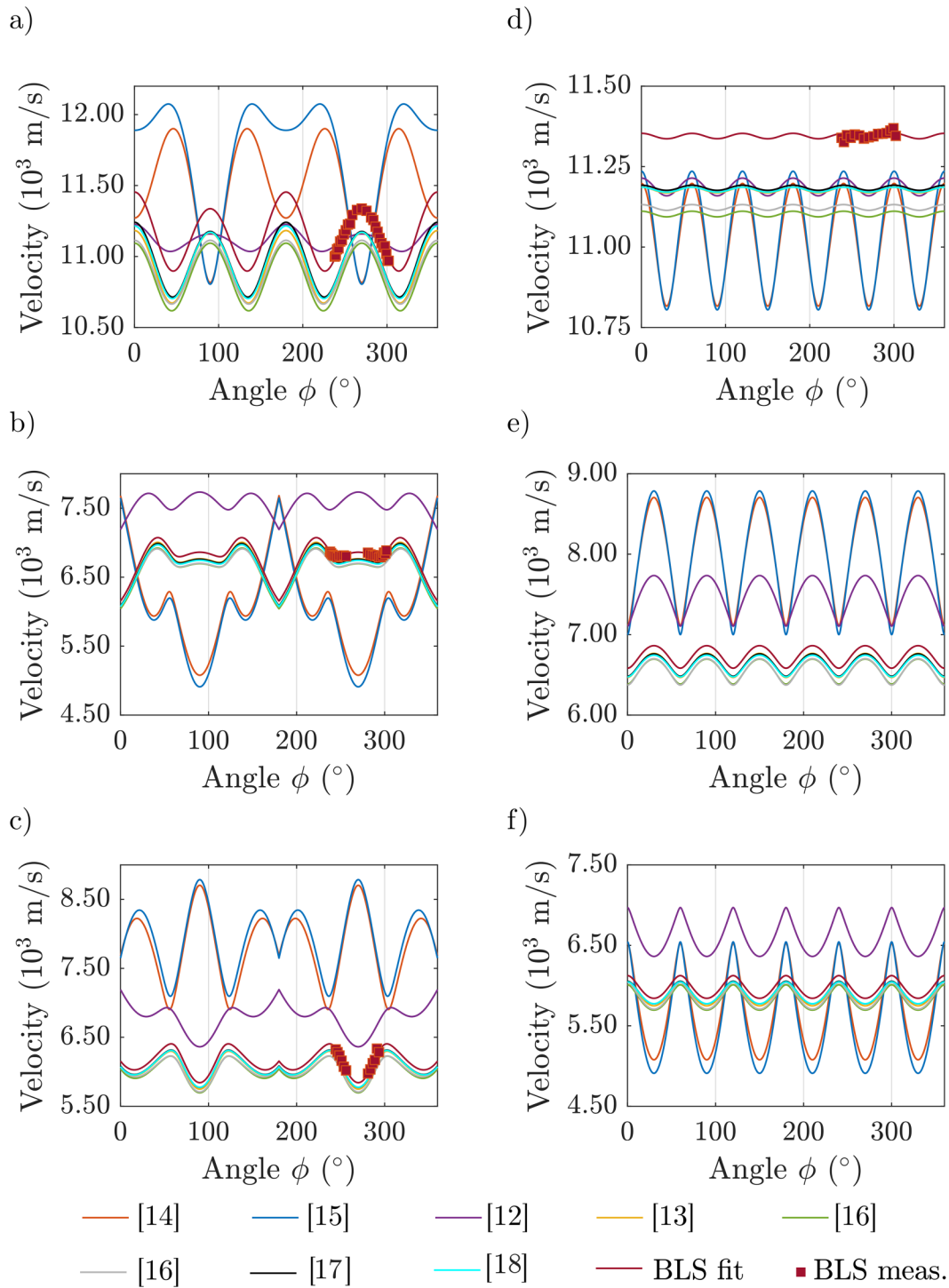
Measuring the ten independent coefficients c_{ij} and e_{ij} may appear a difficult task, especially when using a single wafer or crystal cut. O'Brien *et al.*⁴ reported a BLS study in a single crystal of ferroelectric lithium niobate. Experiments were

performed using a high-resolution grating spectrograph (in 90-scattering geometry) and considering different simple orientations of the specimen to be able to obtain the full elastic and piezoelectric tensors. Compared to the nonlinear least-square fit procedure, considering pure phonon modes simplifies the Christoffel tensor and orthogonalizes the estimation of the different tensor elements. The four phonon directions (100), (010), (001), and (011) provided 11 frequency measurements



11 November 2023 17:04:12

FIG. 4. Velocity curves for X-cut sapphire are shown for (a) the XZ plane and (b) the XY plane. Experimental velocities obtained with BLS are shown with markers. Solid lines are for theoretical velocity curves obtained from the fitted material constants.



11 November 2023 17:04:12

FIG. 5. Comparison of experimental phonon velocities to different sets of materials' constants for sapphire. Velocity curves are shown with solid lines for the XZ plane for (a) the QL phonon, (b) the QS1 phonon, and (c) the QS2 phonon, and for the XY plane for (d) the QL phonon, (e) the QS1 phonon, and (f) the QS2 phonon. They were obtained for the sets of materials' constants listed in Table I. The green line indicates Bernstein pulse-echo and the gray line Bernstein resonance measurements. Experimental velocities are shown with markers.

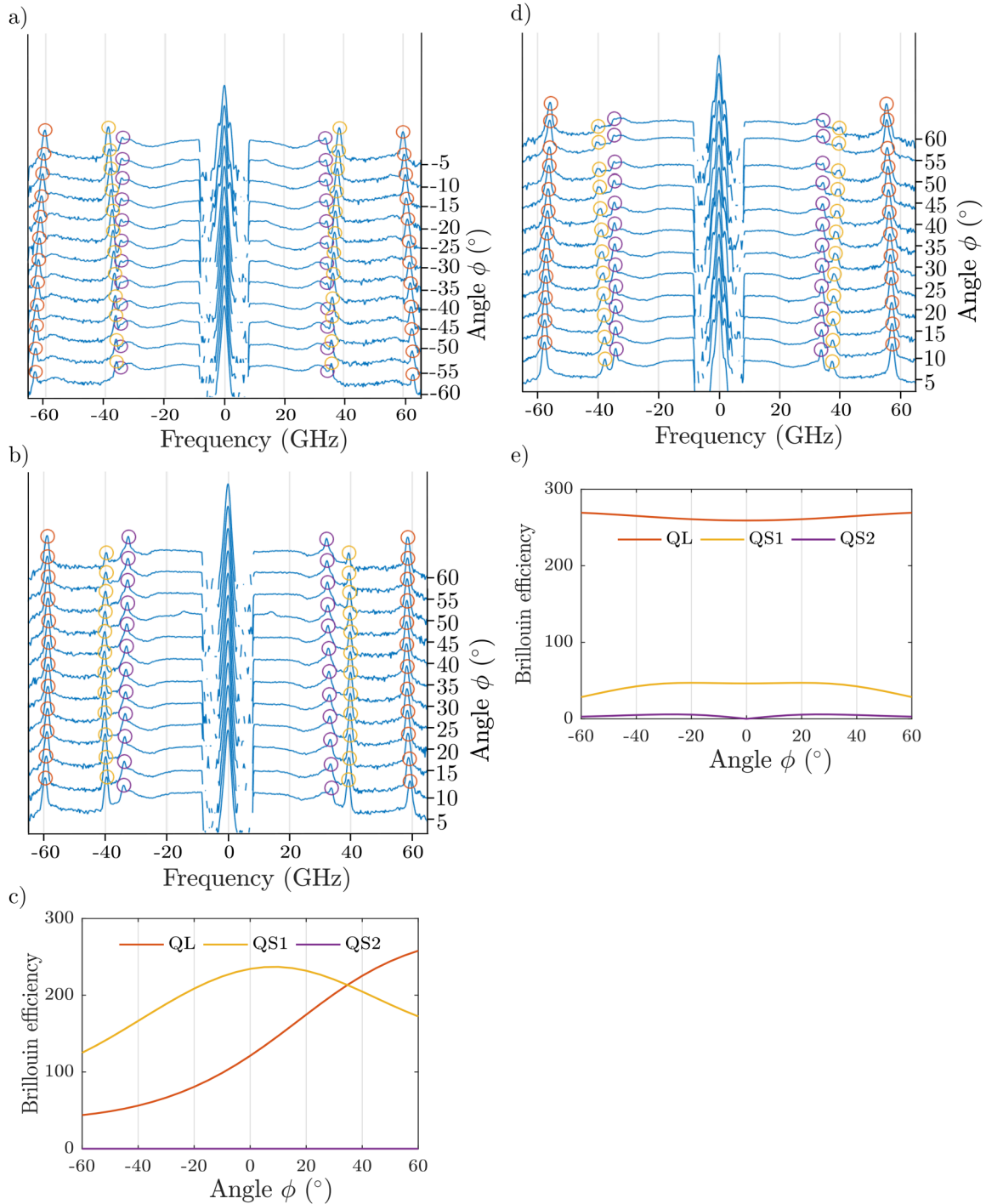
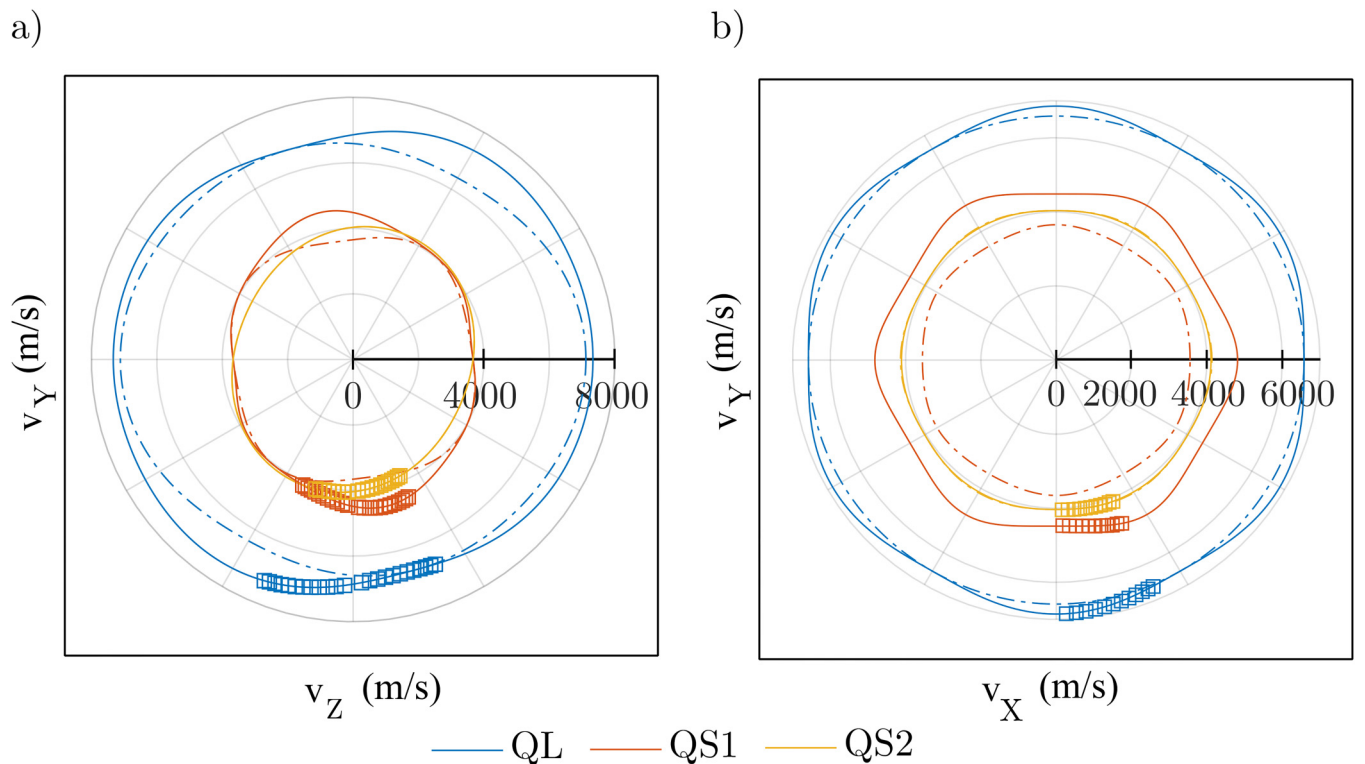


FIG. 6. BLS experimental results for a Y-cut lithium niobate wafer. BLS spectra are shown for the YZ plane for (a) negative and (b) positive values of the angle of incidence ϕ . Theoretical phonon frequencies are shown with circular markers (orange: QL phonon; yellow: QS1 phonon; purple: QS2 phonon). The theoretical photoelastic response is shown in (c) as a function of the angle of incidence ϕ . BLS spectra are shown for the YX plane for (d) positive values of the angle of incidence ϕ . Theoretical phonon frequencies are shown with circular markers (orange: QL phonon; yellow: QS1 phonon; purple: QS2 phonon). The theoretical photoelastic response is shown in (e) as a function of the angle of incidence ϕ .

11 November 2023 17:04:12

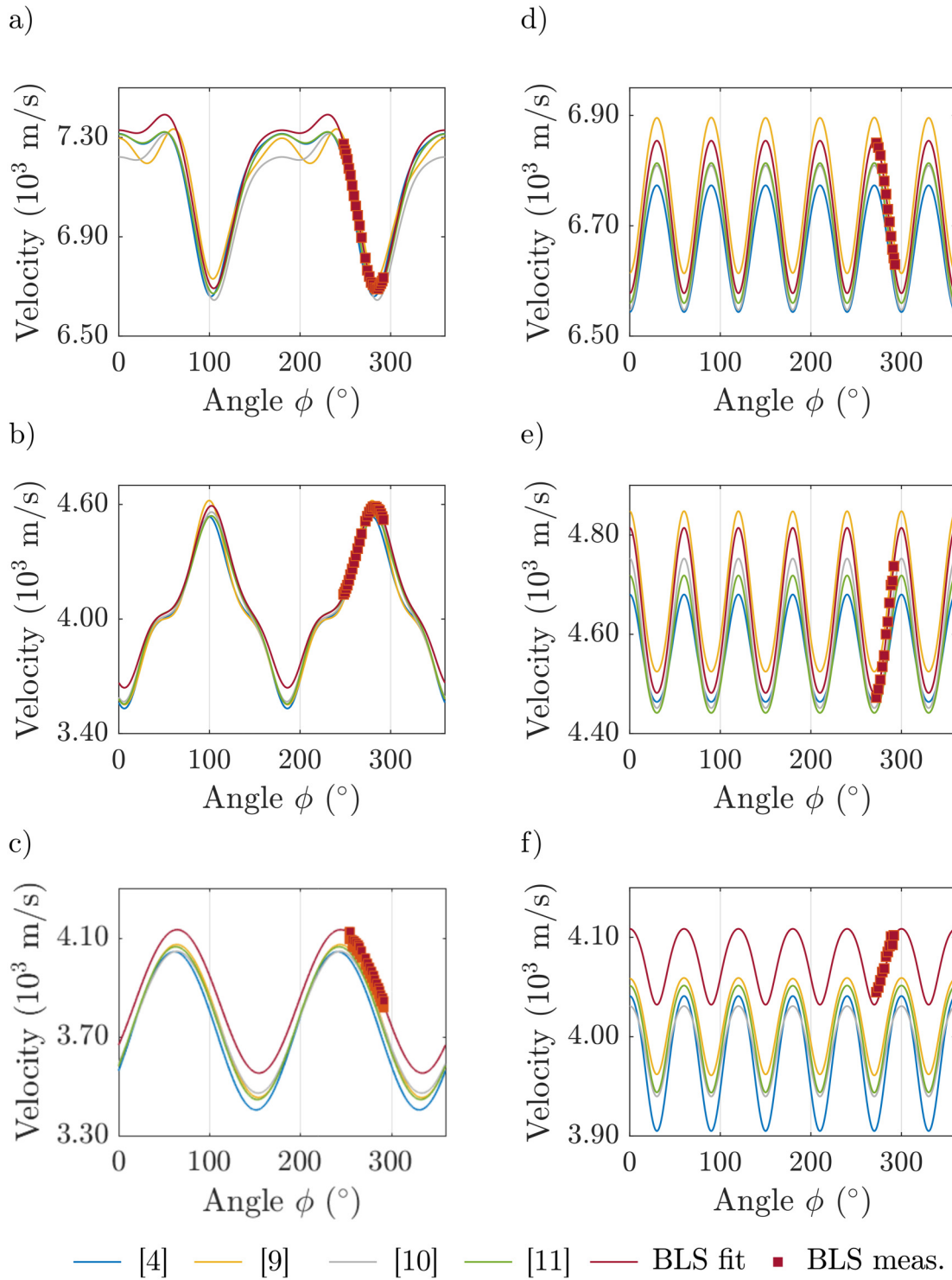
TABLE II. Independent material constants for lithium niobate, taken from the literature^{4,9-11} and obtained by fitting BLS measurements with fixed dielectric constants[†] taken from Ref. 10.

Elastic constants (GPa)					
	O'Brien <i>et al.</i> ⁴	Smith and Welsh ⁹	Kovacs <i>et al.</i> ¹⁰	Ogi <i>et al.</i> ¹¹	BLS
c_{11}	201.25	203.0	198.39	199.5	200.24 ± 0.12
c_{12}	57.91	53.0	54.72	55.27	49.75 ± 0.12
c_{13}	71.08	75.2	65.13	67.67	67.98 ± 0.57
c_{33}	240.10	242.4	227.9	235.0	234.24 ± 2.90
c_{44}	59.63	59.5	59.65	59.48	62.20 ± 0.30
c_{14}	9.43	8.5	7.88	8.70	7.98 ± 0.06
Remaining fit error (GHz)					0.0052
Piezoelectric constants (C/m ²)					
e_{15}	3.705	3.76	3.69	3.65	3.62 ± 0.02
e_{22}	2.264	2.43	2.42	2.39	2.50 ± 0.01
e_{31}	0.53	0.23	0.30	0.31	0.28 ± 0.03
e_{33}	1.71	1.33	1.77	1.72	1.83 ± 0.13
Dielectric constants (ϵ_0)					
ϵ_{11}	44	42.58	45.6	45.05	45.6 [†]
ϵ_{33}	29	42.8	26.3	26.2	26.3 [†]



11 November 2023 17:04:12

FIG. 7. Velocity curves for Y-cut lithium niobate are shown for (a) the YZ plane and (b) the YX plane. Experimental velocities obtained with BLS are shown with markers. Solid lines are for theoretical velocity curves obtained from the fitted material constants. The dotted lines are for theoretical velocity curves obtained similarly but ignoring piezoelectricity.



11 November 2023 17:04:12

FIG. 8. Comparison of experimental phonon velocities to different sets of materials' constants for lithium niobate. Velocity curves are shown with solid lines for the YZ plane for (a) the QL phonon, (b) the QS1 phonon, and (c) the QS2 phonon, and for the YX plane for (d) the QL phonon, (e) the QS1 phonon, and (f) the QS2 phonon. They were obtained for the sets of materials' constants listed in Table II. Experimental velocities are shown with markers.

for 10 independent constants. The values obtained by O'Brien are consistent with ours.

Afterwards, Smith and Welsh⁹ showed that a complete set of coefficients can be obtained from ultrasonic phase-velocity measurements coupled with low-frequency capacitance measurements for the dielectric coefficients. They mentioned that this approach sometimes fails and that then one must measure the electromechanical coupling factor and the natural frequencies of resonating bars. Only six from ten coefficients result from direct measurements. To solve all necessary equations, Smith and Welsh observed that it is inevitable to perform many measurements on many crystals with many orientations.⁹

The characterization of linear elastic, piezoelectric, and dielectric material constants is very important for the fabrication of SAW devices. It can be obtained from precise SAW velocity measurements on a single crystal orientation using a non-linear least squares algorithm, if the SAW velocity of the chosen crystal cut is sensitive to all material constants. Kovacs *et al.* argued that this is the case for 128°-rotated Y-lithium niobate.¹⁰ They measured SAW velocities by scanning the crystal surface with a laser vibrometer along several parallel lines and applying the angular spectrum of waves theory.

Finally, Ogi *et al.*¹¹ proposed a method that yields all ten elastic and piezoelectric coefficients with a single frequency sweep on a single mono-crystal specimen by using acoustic spectroscopy, often called resonance-ultrasound spectroscopy. They identified almost all observed 56 resonance modes by measuring the displacement distributions on a surface using laser-Doppler interferometry. They also mention that the change in elastic stiffness of piezoelectric materials is caused by the dependent combination of piezoelectric and dielectric coefficients, thereby mechanical spectroscopy cannot be used for their separate measurements. This property is also present with BLS measurements. Resonance-ultrasound spectroscopy is very sensitive to the dimensions of the sample and to boundary conditions, limitations that are not present with bulk BLS measurements.

Summarizing, performing BLS measurements on a lithium niobate Y-cut wafer, and using a fitting procedure (with an initial guess for the constants), we were able to estimate the full elastic and piezoelectric tensors with high fit confidence. The technique is contactless and non destructive. It requires prior knowledge of the optical indices of refraction and of the low-frequency dielectric constants. From the obtained set of constants, one can notice that our value for c_{12} is lower compared to previously reported values whereas the value for c_{44} is comparatively larger. Regarding piezoelectric constants, the values we obtain are closest to those of Kovacs *et al.*¹⁰ and Ogi *et al.*¹¹

IV. CONCLUSION

Brillouin light scattering allows one to estimate the elastic tensor of an anisotropic crystal given prior information on the crystal class and on the optical indices of refraction, and on the dielectric tensor at low frequency for piezoelectric crystals. In this paper, we have reported measurements on two anisotropic media with trigonal crystal symmetry: non-piezoelectric sapphire ($\bar{3}m$ point group) and piezoelectric lithium niobate (3 m point group).

Implementing a general fitting procedure to the velocity surfaces for acoustic phonons, we have obtained all six independent elastic-stiffness coefficients of sapphire with a single X-cut wafer, and all six elastic and four piezoelectric coefficients of lithium niobate with a single Y-cut wafer. Standard deviations are small, indicating that confidence in the estimated tensor values is high and that the velocity surfaces can be fitted assuming only crystal symmetry. For the complete estimation of an independent tensor elements, a photoelastic signal for all three acoustic phonons, or elastic waves, is required. Finally, these results were compared to those reported in the literature using ultrasonic means or BLS. We found the best agreement with values obtained by Gladden *et al.*¹⁷ for sapphire and by Ogi *et al.*¹¹ for lithium niobate. Extension of the technique to other crystal cuts and compositions is straightforward.

ACKNOWLEDGMENTS

We gratefully acknowledge Sarah Benchabane-Gaiffe and Quentin Micard for generously providing us with lithium niobate and sapphire wafers and Jean-Marc Côte for help with automatizing the experimental setup. This work was supported by the french RENATECH network and its FEMTO-ST technological facility, the EIPHI Graduate School (Grant No. ANR-17-EURE-0002), and Région Bourgogne-Franche-Comté.

AUTHOR DECLARATIONS

Conflict of Interest

The authors have no conflicts to disclose.

Author Contributions

Fehima Ugarak: Data curation (lead); Investigation (lead); Software (equal); Visualization (lead); Writing – original draft (equal); Writing – review & editing (equal). **Julio A. Iglesias Martínez:** Data curation (supporting); Investigation (supporting); Methodology (supporting); Resources (supporting); Software (supporting); Validation (equal); Writing – review & editing (equal). **Alexis Mosset:** Data curation (supporting); Funding acquisition (supporting); Investigation (supporting); Methodology (supporting); Resources (lead); Supervision (supporting); Validation (supporting); Writing – review & editing (supporting). **Vincent Laude:** Conceptualization (lead); Data curation (supporting); Formal analysis (equal); Funding acquisition (lead); Methodology (equal); Project administration (lead); Software (equal); Supervision (lead); Validation (equal); Writing – original draft (equal); Writing – review & editing (equal).

DATA AVAILABILITY

The data that support the findings of this study are available from the corresponding author upon reasonable request.

REFERENCES

- ¹A. Authier, "International tables for crystallography," in *Physical Properties of Crystals*, edited by A. Authier (Kluwer Academic Publishers, 2006), Vol. D, Chap. 1.1. Introduction to the properties of tensors, pp. 3–33.
- ²D. Royer and E. Dieulesaint, *Elastic Waves in Solids* (Wiley, New York, 1999).

- ³A. O. Krushynska, D. Torrent, A. M. Aragón, R. Ardito, O. R. Bilal, B. Bonello, F. Bosia, Y. Chen, J. Christensen, A. Colombi, and S. A. Cummer, "Emerging topics in nanophononics and elastic, acoustic, and mechanical metamaterials: An overview," *Nanophotonics* **12**, 659–686 (2023).
- ⁴R. O'Brien, G. Rosasco, and A. Weber, "Brillouin scattering in lithium niobate," in *Light Scattering Spectra of Solids: Proceedings of the International Conference held at New York University, New York, 3–6 September 1968* (Springer, 1969), pp. 623–630.
- ⁵F. Scarponi, S. Mattana, S. Corezzi, S. Caponi, L. Comez, P. Sassi, A. Morresi, M. Paolantoni, L. Urbanelli, C. Emiliani, and L. Roscini, "High-performance versatile setup for simultaneous Brillouin-Raman microspectroscopy," *Phys. Rev. X* **7**, 031015 (2017).
- ⁶G. Carloti, "Elastic characterization of transparent and opaque films, multilayers and acoustic resonators by surface Brillouin scattering: A review," *Appl. Sci.* **8**, 124 (2018).
- ⁷F. Kargar and A. A. Balandin, "Advances in Brillouin–Mandelstam light-scattering spectroscopy," *Nat. Photonics* **15**, 720–731 (2021).
- ⁸O. Florez, G. Arregui, M. Albrechtsen, R. Ng, J. Gomis-Bresco, S. Stobbe, C. Sotomayor-Torres, and P. D. García, "Engineering nanoscale hypersonic phonon transport," *Nat. Nanotechnol.* **17**, 947–951 (2022).
- ⁹R. Smith and F. Welsh, "Temperature dependence of the elastic, piezoelectric, and dielectric constants of lithium tantalate and lithium niobate," *J. Appl. Phys.* **42**, 2219–2230 (1971).
- ¹⁰G. Kovacs, M. Anhorn, H. Engan, G. Visintini, and C. Ruppel, "Improved material constants for LiNbO₃ and LiTaO₃," in *IEEE Symposium on Ultrasonics* (IEEE, 1990), pp. 435–438.
- ¹¹H. Ogi, Y. Kawasaki, M. Hirao, and H. Ledbetter, "Acoustic spectroscopy of lithium niobate: Elastic and piezoelectric coefficients," *J. Appl. Phys.* **92**, 2451–2456 (2002).
- ¹²W. G. Mayer and E. Hiedemann, "Optical methods for the ultrasonic determination of the elastic constants of sapphire," *J. Acoust. Soc. Am.* **30**, 756–760 (1958).
- ¹³J. B. Wachtman Jr, W. E. Tefft, D. G. Lam Jr, and R. P. Stinchfield, "Elastic constants of synthetic single crystal corundum at room temperature," *J. Res. Natl. Bur. Stand. Sect. A, Phys. Chem.* **64**, 213 (1960).
- ¹⁴R. V. G. Sundara Rao, "Elastic constants of alumina," *Proc. Indian Acad. Sci., Sect. A* **29**, 352 (1949).
- ¹⁵J. Bhimasenachar, "Elastic constants of corundum," *Curr. Sci.* **18**, 372–373 (1949).
- ¹⁶B. T. Bernstein, "Elastic constants of synthetic sapphire at 27°C," *J. Appl. Phys.* **34**, 169–172 (1963).
- ¹⁷J. R. Gladden, J. H. So, J. D. Maynard, P. W. Saxe, and Y. Le Page, "Reconciliation of ab initio theory and experimental elastic properties of Al₂O₃," *Appl. Phys. Lett.* **85**, 392–394 (2004).
- ¹⁸D. B. Hovis, A. Reddy, and A. H. Heuer, "X-ray elastic constants for α -Al₂O₃," *Appl. Phys. Lett.* **88**, 131910 (2006).
- ¹⁹R. Vacher and E. Courtens, "International tables for crystallography," in *Physical Properties of Crystals*, edited by A. Authier (Kluwer Academic Publishers, 2006), Vol. D, Chap. 2.4. Brillouin scattering, pp. 329–335.
- ²⁰S. T. Bailey, M. D. Twa, J. C. Gump, M. Venkiteshwar, M. A. Bullimore, and R. Sooryakumar, "Light-scattering study of the normal human eye lens: Elastic properties and age dependence," *IEEE Trans. Biomed. Eng.* **57**, 2910–2917 (2010).
- ²¹D. Faurie, N. Girodon-Boulandet, A. Kaladjian, F. Challali, G. Abadías, and P. Djemia, "Setup for high-temperature surface Brillouin light scattering: Application to opaque thin films and coatings," *Rev. Sci. Instrum.* **88**, 023903 (2017).
- ²²M. Grimsditch and A. Ramdas, "Brillouin scattering in diamond," *Phys. Rev. B* **11**, 3139 (1975).
- ²³J. Liu and Y.-J. Jiang, "Brillouin scattering study on elastic and piezoelectric properties of laser irradiated ZnO single crystals," *Chin. Phys. B* **19**, 116201 (2010).
- ²⁴D. Shuo, Z. Yong, L. Yu-Long, G. Siu, C. Lee, and J. Yi-Jian, "Elastic and piezoelectric properties of Ce:BaTiO₃ single crystals," *Chin. Phys. Lett.* **22**, 1790 (2005).
- ²⁵A. B. Singaraju, D. Bahl, and L. L. Stevens, "Brillouin light scattering: Development of a near century-old technique for characterizing the mechanical properties of materials," *AAPS PharmSciTech* **20**, 1–16 (2019).
- ²⁶Z. Meng, T. Thakur, C. Chitrakar, M. K. Jaiswal, A. K. Gaharwar, and V. V. Yakovlev, "Assessment of local heterogeneity in mechanical properties of nanostructured hydrogel networks," *ACS Nano* **11**, 7690–7696 (2017).
- ²⁷R. Mock, B. Hillebrands, and J. R. Sandercock, "Construction and performance of a Brillouin scattering set-up using a triple-pass tandem Fabry-Perot interferometer," *J. Phys. E: Sci. Instrum.* **20**, 656 (1987).
- ²⁸F. Palombo and D. Fioretto, "Brillouin light scattering: Applications in biomedical sciences," *Chem. Rev.* **119**, 7833–7847 (2019).
- ²⁹M. Philipp, U. Müller, R. Sanctuary, P. Seck, and J.-K. Krüger, "Scanning Brillouin microscopy: Acoustic microscopy at gigahertz frequencies," *Arch. Sci. Nat., Phys. Math.* **NS 46**, 11–25 (2012).
- ³⁰R. J. J. Rioboó, N. Gontán, D. Sanderson, M. Desco, and M. V. Gómez-Gavero, "Brillouin spectroscopy: From biomedical research to new generation pathology diagnosis," *Int. J. Mol. Sci.* **22**, 8055 (2021).
- ³¹D. Kajewski, S. Oh, J.-H. Ko, A. Majchrowski, A. Bussmann-Holder, R. Sitko, and K. Roleder, "Brillouin light scattering in niobium doped lead zirconate single crystal," *Sci. Rep.* **12**, 13066 (2022).
- ³²L. La Spina, Q. Micard, A. Mosset, S. Margueron, A. Bartaszyte, and V. Laude, "Dispersion of surface elastic waves on Z-LiNbO₃ films on Z-sapphire," *Appl. Phys. Lett.* **122**, 172202 (2023).
- ³³K. Shemer, G. Bashan, E. Zehavi, H. H. Diamandi, A. Bernstein, K. Sharma, Y. London, D. Barrera, S. Sales, A. Bergman, and A. Zadok, "Optical fiber point sensors based on forward Brillouin scattering," *Opt. Express* **30**, 39321–39328 (2022).
- ³⁴V. Laude, *Phononic Crystals: Artificial Crystals for Sonic, Acoustic, and Elastic Waves*, 2nd ed. (De Gruyter, Berlin, 2020).
- ³⁵R. Weis and T. Gaylord, "Lithium niobate: Summary of physical properties and crystal structure," *Appl. Phys. A* **37**, 191–203 (1985).
- ³⁶A. C. DeFranzo and B. G. Pazol, "Index of refraction measurement on sapphire at low temperatures and visible wavelengths," *Appl. Opt.* **32**, 2224–2234 (1993).
- ³⁷R. M. Waxler and E. N. Farabaugh, "Photoelastic constants of ruby," *J. Res. Natl. Bur. Stand. Sect. A, Phys. Chem.* **74**, 215 (1970).